Electron-phonon processes of the nitrogen-vacancy center in diamond

Taras Plakhotnik,[1,*] Marcus W. Doherty,[2] and Neil B. Manson[2]

[1]*School of Mathematics and Physics, The University of Queensland, Saint Lucia, Queensland 4072, Australia*

[2]*Laser Physics Centre, Research School of Physics and Engineering, Australian National University,*
Australian Capital Territory 2601, Australia

(Received 29 January 2015; revised manuscript received 8 July 2015; published 21 August 2015)

Applications of the negatively charged nitrogen-vacancy center in diamond exploit the center's unique optical and spin properties, which at ambient temperature are predominantly governed by electron-phonon interactions. Here, we investigate these interactions at ambient and elevated temperatures by observing the motional narrowing of the center's excited-state spin resonances. We determine that the center's Jahn-Teller dynamics are much slower than currently believed and that they do not solely account for the broadening of the center's optical resonance above cryogenic temperatures. We show that the inclusion of interactions with symmetric phonon modes can explain the observed broadening and resolve the current inconsistencies in the literature. However, our model also reveals unexpected features of the electron-phonon processes that coincide with other poorly understood vibronic features of the center and require further investigation.

The negatively charged nitrogen-vacancy (NV) center is a point defect in diamond [1] that has found diverse applications in quantum technology. The center is employed as a highly sensitive nanoscale sensor of electromagnetic fields [2–7], temperature [8–13], pressure [14], and rotation [15–18] that can operate in ambient and extreme conditions. In quantum information science, the NV center is used to realize spin registers [19–21] at room temperature and spin-photon entanglement [22,23] at cryogenic temperatures. Recent proposals seek to exploit spin-phonon coupling to enhance NV spin registers and develop novel quantum devices [24–27].

The applications of the NV center are based upon its remarkable optical and spin properties: bright optical fluorescence, long-lived ground-state spin coherence, and methods of optical spin polarization and readout. The latter enable the optical detection of the center's magnetic resonances (ODMR) and are the consequence of spin-dependent phonon-mediated intersystem crossings (ISCs) [28,29]. The center's cryogenic applications also employ the coherence of the center's visible zero-phonon line (ZPL). The necessity of cryogenics arises from the temperature-dependent electron-phonon induced dephasing and depolarization of the ZPL [30,31]. Electron-phonon coupling is also responsible for the motional narrowing of the center's excited-state spin resonances, which determines their utility as an additional quantum resource for sensing and information processing [13,32]. Thus, a thorough understanding of the NV center's electron-phonon interactions is important to the continued advancement of its applications and may be generalized to similar defects with emerging quantum applications [33–36]. Here, we identify several issues in the current understanding and propose possible resolutions.

The electronic structure of the NV center is depicted in Fig. 1. The optical transitions of the visible ZPL occur between the ground $^3A_2$ and excited ^3E spin triplet levels. The temperature-dependent broadening of the ZPL was initially described [30] using the widely applicable model of quadratic

electron-phonon interactions with A_1 phonon modes [37]. However, subsequent single center cryogenic measurements revealed that the broadening was more consistent with the characteristic $\propto T^5$ temperature dependence of linear electron-phonon (Jahn-Teller) interactions with E phonon modes [31]. These interactions induce population transfer between the quasidegenerate orbital states ($|X\rangle$, $|Y\rangle$) of the ^3E level (see Fig. 1), which dephases the optical transitions and leads to the depolarization of the ZPL fluorescence [31]. Applying their Jahn-Teller model, Fu *et al.* [31] identified a factor of ~2 inconsistency between the population transfer rates that describe the ZPL broadening and depolarization at low temperatures. By introducing a phonon cutoff energy, Abtew *et al.* [38] extended Fu *et al.*'s ZPL broadening model up to room temperature. In doing so, they obtained a cutoff at 50 meV for E phonons, which is much lower than the diamond Debye energy $\Omega_D \approx 168$ meV [39] and the energy $\Omega_V \approx 64$ meV of the main feature of the electron-phonon spectral density extracted from the center's visible phonon sideband [40].

At temperatures $\lesssim$30 K, the complicated six level ^3E fine structure (see Fig. 1) is observed via high-resolution optical spectroscopy [28]. Above $\approx$150 K [41], the population transfer between the ^3E orbital states is sufficiently fast to dynamically average the ^3E fine structure so that its ODMR resembles the simpler three level structure of the ground state [42]. The dynamically averaged fine structure is temperature dependent and is described by the spin Hamiltonian [13]

$$H = D_\parallel \left(S_z^2 - \frac{2}{3} \right) - D_\perp R(T) \left(S_x^2 - S_y^2 \right) \qquad (1)$$

where $D_\parallel = 1.42$ GHz and $D_\perp = 0.775$ GHz are the ^3E spin-spin parameters; $R(T) = (e^{h\xi_\perp/k_BT} - 1)/(e^{h\xi_\perp/k_BT} + 1)$ is the temperature reduction factor that approaches zero in the limit $k_BT \gg h\xi_\perp$; h and k_B are the Planck and Boltzman constants, respectively; and $\xi_\perp$ is the ^3E strain splitting.

The dynamical averaging is also expected to motionally narrow the ^3E ODMR, since the rapid population transfer decouples the orbit and spin degrees of freedom. Fuchs *et al.* have measured the ^3E spin dephasing rate at room
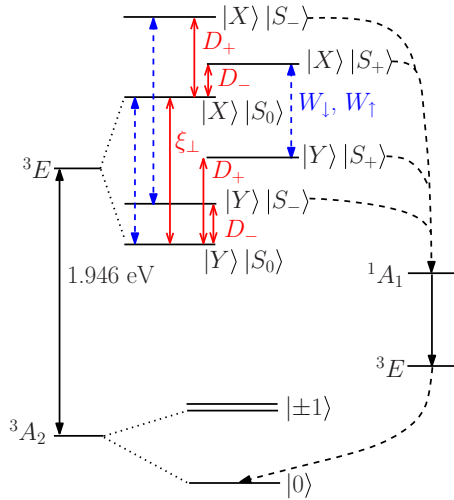
————
*taras@physics.uq.edu.au

FIG. 1. (Color online) The electronic and fine structures of the NV center at high stress. The ^3E sublevels are labeled by their product of orbital ($|X\rangle$, $|Y\rangle$) and spin ($|0\rangle$, $|S_\pm\rangle$) states, where the spin states are solutions of Eq. (1). The ^3E fine-structure splittings ($D_\pm = D_\parallel \pm D_\perp$) are denoted in red. The $^3A_2$ sublevels are denoted by their spin projection ($m_s = 0, \pm 1$). The optical transitions of the spin triplet and singlet levels are depicted as two solid arrows on the right and left sides of the diagram. The visible ZPL is at 1.946 eV. Blue dashed arrows represent the population transfers within ^3E (rates $W_\downarrow$ and $W_\uparrow$). The black dashed arrows denote the allowed ISCs between the spin triplet and singlet levels.

temperature [32]. They attributed the observed dephasing to the dynamical averaging process and, using a motional narrowing model, suggested that elevated temperatures or strain may decrease its rate. However, their proposal is yet to be tested by a systematic study of the motional narrowing effect. Furthermore, there is an inconsistency between Fuchs *et al.*'s observations and the current ZPL broadening model. If the population transfer rate (~10 THz) at room temperature is inferred from the ZPL width [31], then the spin dephasing rate predicted by the motional narrowing model (~1.2 MHz) is almost two orders of magnitude smaller than measured (~92 MHz). The unexplained low cutoff of Abtew *et al.*, the discrepancy identified by Fu *et al.*, the conspicuous absence of interactions with A_1 modes, and the much larger than expected ^3E spin dephasing rate all indicate problems in the current ZPL broadening model.

In this Rapid Communication, we report observations of the ^3E ODMR of NV centers in nanodiamond over the temperature range 295–550 K. We show that the ODMR is well described by a motional narrowing model and extract the population transfer rates. We establish that the rates are much slower than currently believed and do not account for the observed ZPL broadening at room temperature. We propose that quadratic interactions with A_1 phonons are responsible for the additional broadening and we successfully fit an acoustic model of the E and A_1 electron-phonon interactions to the combined data set of our population transfer rate measurements and Fu *et al.*'s measurements of the ZPL depolarization and broadening. Our fit yields unexpected features of the electron-phonon interactions that coincide with other poorly understood vibronic

features of the NV center and motivate further investigation. Consequently, our results support and rectify the proposals of Fuchs *et al.*, resolve the inconsistencies of the ZPL broadening model, and provide valuable insight into NV electron-phonon interactions above cryogenic temperatures. The latter is notably required to validate the recent model of the center's spin-selective ISCs [28,29] and to extend it to room temperature.

Our continuous-wave ODMR experiments were performed using 532-nm laser excitation and fluorescence collection via an epifluorescence design. The nanodiamonds were spin coated on a silica substrate. The NV spin resonances were driven by a radio-frequency (rf) magnetic field created by a gold wire deposited onto the substrate. The excitation laser spot overlapped with the wire and the optical heating of the wire was used to control the temperature of a chosen nanodiamond. As described in [13], the temperature of the nanodiamond was measured using the NV center's optical Debye-Waller factor with an error less than 3%. Other experimental details are as per [13]. On average, the nanodiamonds had a diameter of ~30 nm and contained ~15 NV centers. We performed ODMR measurements on a total of ten nanodiamonds (see [43] for summary). The results from one nanodiamond are presented here and are consistent with the rest of the sample and, as will be explained, measurements in bulk diamond. Previous optical spectroscopy has measured the ^3E strain splitting of the nanodiamond to be $h\xi_\perp \sim 4.7$ meV [13]. This large strain splitting permits a simple ^3E fine structure (see Fig. 1) where the spin resonances of the ^3E orbital states are approximately equal and thus a simple application of the motional narrowing model. Note that the strain splittings in [31,32] were much smaller.

Examples of ODMR spectra are shown in Fig. 2. Averaging over the unresolved ^3E hyperfine structure, the observed ODMR splitting is [13]

$$\Delta_{\text{ODMR}} = \frac{2}{3}D_\perp R(T) + \frac{4}{3}[A^2 + D_\perp^2 R^2(T)]^{1/2}, \qquad (2)$$

where $A \approx 40$ MHz is the isotropic hyperfine parameter. The rf-power broadening is evident in Fig. 2. Similar to the analysis
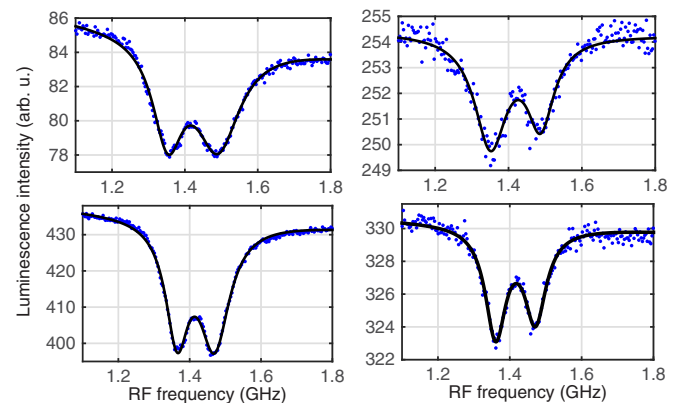

FIG. 2. (Color online) Example ODMR spectra at different temperatures (315 K upper, 455 K lower) and RF powers (440 mW left, 55 mW right). The narrowing and reduced splitting of the lines at higher temperature as well as power broadening at higher RF power can be seen. The line-shape fits (solid lines) are the sum of two Lorentzians and a linear background.

of the $^3A_2$ ODMR in [44], a five-level model of the optical and spin dynamics yields the following expressions for the ODMR linewidth Γ_{ODMR} and contrast C_{ODMR}:

$$\Gamma_{\mathrm{ODMR}} = \Gamma_{\mathrm{ODMR}}^{\mathrm{(inh)}} + \Gamma_{\mathrm{ODMR}}^{\mathrm{(h)}} \left(1 + \frac{4\pi\kappa P_{\mathrm{rf}}}{\Gamma_{\mathrm{ODMR}}^{\mathrm{(h)}} \gamma_1} \right)^{1/2},$$

$$C_{\mathrm{ODMR}} = C_{\mathrm{ODMR}}^{\mathrm{(max)}} \frac{4\pi\kappa P_{\mathrm{rf}}}{4\pi\kappa P_{\mathrm{rf}} + \gamma_1 \Gamma_{\mathrm{ODMR}}^{\mathrm{(h)}}}, \quad (3)$$

where $\Gamma_{\mathrm{ODMR}}^{\mathrm{(h)}}$ and $\Gamma_{\mathrm{ODMR}}^{\mathrm{(inh)}}$ are the homogenous and inhomogenous linewidths in the absence of power broadening, P_{rf} is the rf power, κ is a proportionality factor such that κP_{rf} is the spin Rabi frequency, and γ_1 is the effective spin relaxation rate. The essential difference to [44] is a much weaker but more complicated dependence of γ_1 on the laser power. At low laser powers, $\gamma_1 \approx k k_{\mathrm{ISC}}/(k + 0.5k_{\mathrm{ISC}}) \approx 22$ MHz, where $k \approx 20$ MHz [45] is the ^3E radiative decay rate in nanodiamond of the relevant type and origin and $k_{\mathrm{ISC}} \approx 50$ MHz is the average ^3E ISC rate [28,45]. Stress inhomogeneity and the unresolved hyperfine structure contribute to $\Gamma_{\mathrm{ODMR}}^{\mathrm{(inh)}}$.

The homogenous linewidth $\Gamma_{\mathrm{ODMR}}^{\mathrm{(h)}} = \Gamma_\infty + \Gamma_{\mathrm{MN}}(T)$ is the sum of the broadening due to the ^3E orbital decay rate $\Gamma_\infty = (k + 0.5k_{\mathrm{ISC}})/\pi$ and motional narrowing $\Gamma_{\mathrm{MN}}(T)$. While the orbital decay rate increases at high temperature [8,46], this temperature dependence is ignored in the following because the contribution of Γ_∞ to the observed Γ_{ODMR} changes little, from 14 to 17 MHz between 295 and 500 K. The spin bath dephasing contribution to Γ_∞ is also ignored because it has been assessed using the $^3A_2$ ODMR to be negligibly small (1–2 MHz). In the fast exchange approximation of motional narrowing [43], where the population transfer rates ($W_\uparrow$, $W_\downarrow$) are much larger than the jump in the spin resonances between the ^3E orbital states ($2D_\perp$), $\Gamma_{\mathrm{MN}}(T) \approx \beta(T) 2\pi D_\perp^2/W_\downarrow$. The factor $\beta(T) = 8e^{-h\xi_\perp/k_B T}/(e^{-h\xi_\perp/k_B T} + 1)^3$ is close to 1 above room temperatures. Thus, as $W_\downarrow$ increases with temperature, Γ_{MN} decreases.

In the temperature regime $k_B T \gg h\xi_\perp$, Raman scattering of E phonons dominates the population transfer rates [29,43]

$$W_\downarrow = B_E T^5 I(T) \quad (4)$$

and $W_\uparrow = W_\downarrow e^{-h\xi_\perp/k_B T}$, where $I(T) = \int_{x_\perp}^{\frac{\Omega_E}{k_B T}} \frac{x^2 e^x (x - x_\perp)^2}{(e^x - 1)(e^{x - x_\perp} - 1)} dx$, $x_\perp = h\xi_\perp/k_B T$, and Ω_E is the cutoff energy for E phonons. The deformation potential and Debye density of states for acoustic phonons have been assumed such that the corresponding electron-phonon spectral density of E phonons is $J_E(\epsilon) \approx \eta_E \epsilon^3$, where ϵ is the phonon energy and η_E is the proportionality constant defined in [29]. The constant $B_E = \frac{64}{\pi} \hbar \eta_E^2 k_B^5$. While in the simplest case $\Omega_E = \Omega_D$, the cutoff is often considered as a phenomenological parameter that signals the departure from $J_E(\epsilon) \propto \epsilon^3$.

Systematic measurements of the ODMR linewidth, contrast and splitting at different temperatures, rf, and laser powers are presented in Fig. 3. The weak optical-power dependence [inset of Fig. 3(a)] supports the approximation $\gamma_1 \approx 22$ MHz. The $\sim T^{-2}$ temperature dependence of the linewidth indicates that the high-temperature regime ($1 \gg x_\perp, \hbar\Omega_E/k_B T$) of the
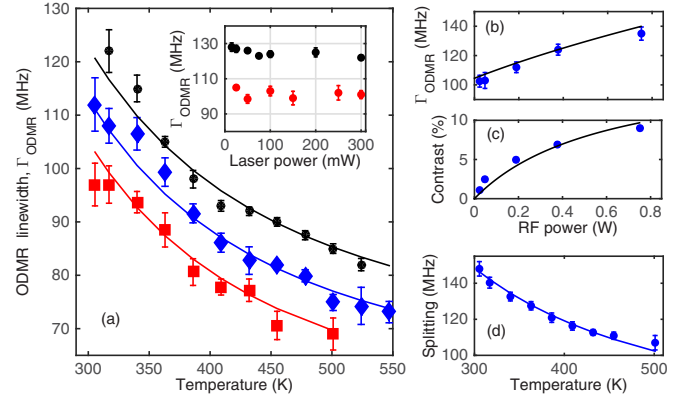

FIG. 3. (Color online) (a) ODMR linewidth as a function of temperature at rf powers of 400, 200, and 50 mW (top to bottom). The inset shows the weak optical power dependence of the linewidth at 294 K and at two rf powers: 47 mW (bottom) and 380 mW (top). (b) and (c) show the rf-power dependence of the linewidth and contrast at 294 K and 100 mW optical power. (d) ODMR splitting at different temperatures (50-mW rf power). Error bars are determined by the statistics of repeated measurements. The plotted linewidth is the average width of the two lines.

population transfer rates is applicable, such that

$$I(T) = \frac{1}{3}\left(\frac{\Omega_E}{k_B T}\right)^3 \left(1 - \frac{h\xi_\perp}{\Omega_E}\right)^2 \left(1 + \frac{h\xi_\perp}{2\Omega_E}\right), \quad (5)$$

$W_\downarrow = Q T^2$, and $\Gamma_{\mathrm{ODMR}}^{\mathrm{(h)}} = \Gamma_\infty + \beta(T) 2\pi D_\perp^2/(Q T^2)$, where Q is a constant.

The simultaneous fitting of the six data sets using the five parameters yields $\Gamma_{\mathrm{ODMR}}^{\mathrm{(inh)}} = 33 \pm 3$ MHz, $\kappa = 210 \pm 40$ MHz^2 W^{-1}, $C_{\mathrm{ODMR}}^{\mathrm{(max)}} = 16 \pm 2\%$, $Q = 0.83 \pm 0.06$ MHz K^{-2}, and $h\xi_\perp = 4.6 \pm 0.2$ meV. The values of κ and $h\xi_\perp$ are in reasonable agreement with the parameters of the rf wire and previous optical spectroscopy, respectively. The fitting yields $\Gamma_{\mathrm{ODMR}}^{\mathrm{(h)}} = 55$ MHz at room temperature. The dephasing rate measured by Fuchs *et al.* in bulk diamond corresponds to $\Gamma_{\mathrm{ODMR}}^{\mathrm{(h)}} \sim 29$ MHz. Taking into account that the much smaller stress splitting $\xi_\perp$ of Fuchs *et al.*'s NV center will increase Q by ~ 2 in accordance with Eq. (5) (using $\Omega_E = 13.4$ meV as later discussed), the two values are in agreement. Hence, we conclude that our nanodiamond measurements are consistent with bulk diamond and capture intrinsic phenomena of the NV center.

The previous measurements of the ZPL width [31] are plotted in Fig. 4 together with $W_\downarrow/(2\pi)$ calculated here using the value of Q that we obtained by fitting our motional narrowing observations [rescaled to $\xi_\perp = 0$ using Eq. (5) to match the stress splitting in [31]]. It is evident that the rates are orders of magnitude too small to account for the ZPL width alone. We propose that the additional width is due to quadratic interactions with A_1 modes that purely dephase the optical transitions [30,37]. In this case, the ZPL width is [47]

$$\Gamma_{\mathrm{ZPL}} = \frac{W_\downarrow}{2\pi} + \frac{W_A}{\pi} + \gamma_0, \quad (6)$$

where W_A is the additional dephasing rate and γ_0 is the approximately temperature-independent contribution of the
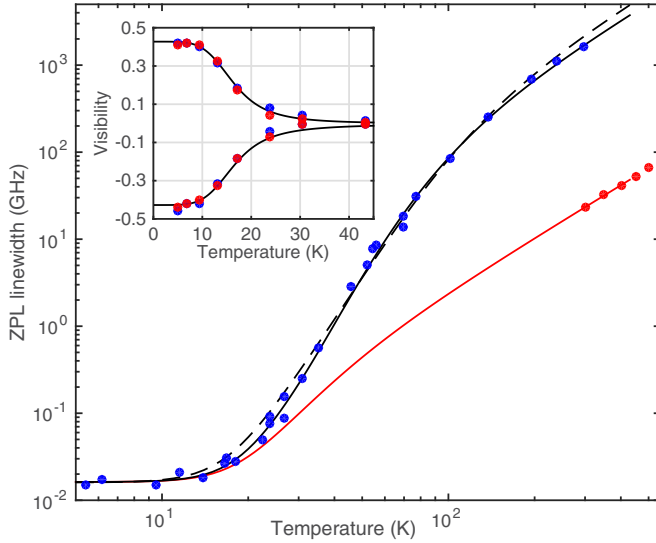
FIG. 4. (Color online) Blue points are the ZPL width measured in [31]. The black solid curve depicts the fit of our model and the black dashed curve is the extended Jahn-Teller model of [38]. The red solid curve is the contribution of $W_\downarrow$ to the ZPL width according to Eqs. (4) and (6). The red dots show $W_\downarrow/2\pi$ derived from ODMR data alone. Inset: the ZPL polarization visibility of two NV centers (red and blue points) from [31]. The solid curve is our fit obtained using the model $V = [W_\uparrow - W_\downarrow \pm r(1-a)/(1+a)]/(W_\downarrow + W_\uparrow + r)$, where $a = 0.40 \pm 0.02$ and $r = 80$ MHz are defined in [31], and $W_\downarrow$ and $W_\uparrow$ are determined by our fit of the ZPL width.

optical decay rate. As per a similar derivation [43] of $W_\downarrow$ and assumption of an acoustic spectral density of A_1 phonons $J_A(\epsilon) \propto \epsilon^3$,

$$W_A = B_A T^7 \int_0^{\frac{\Omega_A}{k_B T}} \frac{e^x x^6}{(e^x - 1)^2} dx, \qquad (7)$$

where B_A is a constant and Ω_A is the cutoff energy of A_1 phonons. We used Eqs. (4), (6), and (7) to fit our $W_\downarrow/2\pi$ measurements and Fu *et al.*'s ZPL width measurements [31] and obtained $B_E = 1.32$ Hz K^{-5}, $\Omega_E = 13.4 \pm 1$ meV,

$B_A = 24 \pm 4$ μHz K^{-7}, $\Omega_A = 37 \pm 2$ meV, and $\gamma_0 = 16.2 \pm 0.5$ MHz (value in bulk diamond). The theoretically expected equality $B_E \Omega_E^3 = 3k_B^3 Q$ holds if Q obtained using Eqs. (4) and (5) is increased by a factor of 1.98 to account for $\xi_\perp \approx 0$ in these crystals. Our fit of the ZPL width better describes the low- and room-temperature regions than the extended Jahn-Teller model of [38]. Additionally, unlike in [31], the parameters (B_E and Ω_E) of the population transfer rates that we obtained from fitting the ZPL width measurements also fit the ZPL polarization visibility measurements (see inset of Fig. 4). Hence, we conclude that our model of the ^3E electron-phonon interactions successfully describes the ZPL broadening and depolarization as well as the ^3E ODMR motional narrowing and thus resolves the inconsistencies of previous models.

Notably, our cutoffs are much lower than the energy where the spectral densities of the $^3A_2$ electron-phonon interactions depart from $\propto \epsilon^3$ [40] and imply that the ^3E spectral densities are significantly different, which is consistent with the asymmetry of the NV center's visible absorption and emission phonon sidebands [1]. Examination of the center's other phonon sidebands (see [43]) reveals that our ^3E phonon cutoffs Ω_E and Ω_A are very similar to the energies of the E and A_1 phonon related vibronic features present in the emission phonon sidebands of both the center's infrared $^1A_1 \rightarrow {}^1E$ transition [48] and the visible $^2A_2 \rightarrow {}^2E$ transition of the center's neutral charge state [49]. As these vibronic features do not occur in the respective absorption phonon sidebands, they are results of electron-phonon interactions within the E electronic levels. Since it is well known that vibronic coupling can modify electronic interactions [50], we believe that it is highly unlikely that this strong similarity of the ^3E phonon cutoffs and the vibronic energies of the other E electronic levels is purely fortuitous. Indeed, the vibronic interactions responsible for the features of the other E electronic levels may manifest as modifications of the ^3E spectral densities. Hence, it is clear that further study of these vibronic features is required to more precisely explain the ^3E phonon cutoffs.

[1] M. W. Doherty, N. B. Manson, P. Delaney, F. Jelezko, J. Wrachtrup, and L. C. L. Hollenberg, Phys. Rep. **528**, 1 (2013).

[2] D. Le Sage, K. Arai, D. R. Glenn, S. J. DeVience, L. M. Pham, L. Rahn-Lee, M. D. Lukin, A. Yacoby, A. Komeili, and R. L. Walsworth, Nature (London) **496**, 486 (2013).

[3] M. S. Grinolds, S. Hong, P. Maletinsky, L. Luan, M. D. Lukin, R. L. Walsworth, and A. Yacoby, Nature Physics **9**, 215 (2013).

[4] H. J. Mamin, M. Kim, M. H. Sherwood, C. T. Rettner, K. Ohno, D. D. Awschalom, and D. Rugar, Science **339**, 557 (2013).

[5] T. Staudacher, F. Shi, S. Pezzagna, J. Meijer, J. Du, C. A. Meriles, F. Reinhard, and J. Wrachtrup, Science **339**, 561 (2013).

[6] F. Dolde, H. Fedder, M. W. Doherty, T. Nöbauer, F. Rempp, G. Balasubramanian, T. Wolf, F. Reinhard, L. C. L. Hollenberg, F. Jelezko, and J. Wrachtrup, Nature Physics **7**, 459 (2011).

[7] F. Dolde, M. W. Doherty, J. Michl, I. Jakobi, B. Naydenov, S. Pezzagna, J. Meijer, P. Neumann, F. Jelezko, N. B. Manson, and J. Wrachtrup, Phys. Rev. Lett. **112**, 097603 (2014).

[8] D. M. Toyli, D. J. Christle, A. Alkauskas, B. B. Buckley, C. G. Van de Walle, and D. D. Awschalom, Phys. Rev. X **2**, 031001 (2012).

[9] D. M. Toyli, C. F. de las Casas, D. J. Christle, V. V. Dobrovitski, and D. D. Awschalom, PNAS **110**, 8417 (2013).

[10] P. Neumann, I. Jakobi, F. Dolde, C. Burk, R. Reuter, G. Waldherr, J. Honert, T. Wolf, A. Brunner, J. H. Shim, D. Suter, H. Sumiya, J. Isoya, and J. Wrachtrup, Nano Lett. **13**, 2738 (2013).

[11] G. Kucsko, P. C. Maurer, N. Y. Yao, M. Kubo, H. J. Noh, P. K. Lo, H. Park, and M. D. Lukin, Nature (London) **500**, 54 (2013).

[12] M. W. Doherty, V. M. Acosta, A. Jarmola, M. S. J. Barson, N. B. Manson, D. Budker, and L. C. L. Hollenberg, Phys. Rev. B **90**, 041201(R) (2014).

[13] T. Plakhotnik, M. W. Doherty, J. H. Cole, R. Chapman, and N. B. Manson, Nano Lett. **14**, 4989 (2014).

[14] M. W. Doherty, V. V. Struzhkin, D. A. Simpson, L. P. McGuinness, Y. Meng, A. Stacey, T. J. Karle, R. J. Hemley, N. B. Manson, L. C. L. Hollenberg, and S. Prawer, Phys. Rev. Lett. **112**, 047601 (2014).

[15] D. Maclaurin, M. W. Doherty, L. C. L. Hollenberg, and A. M. Martin, Phys. Rev. Lett. **108**, 240403 (2012).

[16] M. P. Ledbetter, K. Jensen, R. Fischer, A. Jarmola, and D. Budker, Phys. Rev. A **86**, 052116 (2012).

[17] A. Ajoy and P. Cappellaro, Phys. Rev. A **86**, 062104 (2012).

[18] M. W. Doherty, J. Michl, F. Dolde, I. Jakobi, P. Neumann, N. B. Manson, and J. Wrachtrup, New J. Phys. **16**, 063067 (2014).

[19] M. V. G. Dutt, L. Childress, L. Jiang, E. Togan, J. Maze, F. Jelezko, A. S. Zibrov, P. R. Hemmer, and M. D. Lukin, Science **316**, 1312 (2007).

[20] P. Neumann, N. Mizuochi, F. Rempp, P. Hemmer, H. Watanabe, S. Yamasaki, V. Jacques, T. Gaebel, F. Jelezko, and J. Wrachtrup, Science **320**, 1326 (2008).

[21] G. Waldherr, Y. Wang, S. Zaiser, M. Jamali, T. Schulte-Herbrueggen, H. Abe, T. Ohshima, J. Isoya, J. F. Du, P. Neumann, and J. Wrachtrup, Nature (London) **506**, 204 (2014).

[22] E. Togan, Y. Chu, A. S. Trifonov, L. Jiang, J. Maze, L. Childress, M. V. G. Dutt, A. S. Soerensen, P. R. Hemmer, A. S. Zibrov, and M. D. Lukin, Nature (London) **466**, 730 (2010).

[23] H. Bernien, B. Hensen, W. Pfaff, G. Koolstra, M. S. Blok, L. Robledo, T. H. Taminiau, M. Markham, D. J. Twitchen, L. Childress, and R. Hanson, Nature (London) **497**, 86 (2013).

[24] S. D. Bennett, N. Y. Yao, J. Otterbach, P. Zoller, P. Rabl, and M. D. Lukin, Phys. Rev. Lett. **110**, 156402 (2013).

[25] E. R. MacQuarrie, T. A. Gosavi, N. R. Jungwirth, S. A. Bhave, and G. D. Fuchs, Phys. Rev. Lett. **111**, 227602 (2013).

[26] K. V. Kepesidis, S. D. Bennett, S. Portolan, M. D. Lukin, and P. Rabl, Phys. Rev. B **88**, 064105 (2013).

[27] P. Ovartchaiyapong, K. W. Lee, B. A. Myers, and A. C. Bleszynski Jayich, Nature Comm. **5**, 4429 (2014).

[28] M. L. Goldman, A. Sipahigil, M. W. Doherty, N. Y. Yao, S. D. Bennett, M. Markham, D. J. Twitchen, N. B. Manson, A. Kubanek, and M. D. Lukin, Phys. Rev. Lett. **114**, 145502 (2015).

[29] M. L. Goldman, M. W. Doherty, A. Sipahigil, N. Y. Yao, S. D. Bennett, N. B. Manson, A. Kubanek, and M. D. Lukin, Phys. Rev. B **91**, 165201 (2015).

[30] G. Davies, J. Phys. C **7**, 3797 (1974).

[31] K.-M. C. Fu, C. Santori, P. E. Barclay, L. J. Rogers, N. B. Manson, and R. G. Beausoleil, Phys. Rev. Lett. **103**, 256404 (2009).

[32] G. D. Fuchs, V. V. Dobrovitski, D. M. Toyli, F. J. Heremans, C. D. Weis, T. Schenkel, and D. D. Awschalom, Nat. Phys. **6**, 668 (2010).

[33] B. Pingault, J. N. Becker, C. H. H. Schulte, C. Arend, C. Hepp, T. Godde, A. I. Tartakovskii, M. Markham, C. Becher, and M. Atatüre, Phys. Rev. Lett. **113**, 263601 (2014).

[34] L. J. Rogers, K. D. Jahnke, M. H. Metsch, A. Sipahigil, J. M. Binder, T. Teraji, H. Sumiya, J. Isoya, M. D. Lukin, P. Hemmer, and F. Jelezko, Phys. Rev. Lett. **113**, 263602 (2014).

[35] D. J. Christle, A. L. Falk, P. Andrich, P. V. Klimov, J. Hassan, N. T. Son, E. Janzén, T. Ohshima, and D. D. Awschalom, Nat. Mater. **14**, 160 (2014).

[36] M. Widmann, S.-Y. Lee, T. Rendler, N. Tien Son, H. Fedder, S. Paik, L.-P. Yang, N. Zhao, S. Yang, I. Booker, A. Denisenko, M. Jamali, S. A. Momenzadeh, I. Gerhardt, T. Ohshima, A. Gali, E. Janzén, and J. Wrachtrup, Nat. Mater. **14**, 164 (2014).

[37] A. A. Maradudin, *Solid State Physics*, edited by F. Seitz and D. Turnbull, Vol. 18 (Academic Press, New York, 1966), pp. 273–420.

[38] T. A. Abtew, Y. Y. Sun, B.-C. Shih, P. Dev, S. B. Zhang, and P. Zhang, Phys. Rev. Lett. **107**, 146403 (2011).

[39] A. M. Zaitsev, *Optical Properties of Diamond: A Data Handbook* (Springer, New York, 2001).

[40] P. Kehayias, M. W. Doherty, D. English, R. Fischer, A. Jarmola, K. Jensen, N. Leefer, P. Hemmer, N. B. Manson, and D. Budker, Phys. Rev. B **88**, 165202 (2013).

[41] A. Batalov, V. Jacques, F. Kaiser, P. Siyushev, P. Neumann, L. J. Rogers, R. L. McMurtrie, N. B. Manson, F. Jelezko, and J. Wrachtrup, Phys. Rev. Lett. **102**, 195506 (2009).

[42] L. J. Rogers, R. L. McMurtrie, M. J. Sellars, and N. B. Manson, New J. Phys. **11**, 063007 (2009).

[43] See Supplemental Material at http://link.aps.org/supplemental/10.1103/PhysRevB.92.081203 for a summary of measurements, derivations of the motional narrowing model and electron-phonon transition rates, and discussion of the NV center's vibronic features.

[44] K. Jensen, V. M. Acosta, A. Jarmola, and D. Budker, Phys. Rev. B **87**, 014115 (2013).

[45] R. Chapman and T. Plakhotnik, Phys. Rev. B **86**, 045204 (2012).

[46] T. Plakhotnik and D. Gruber, Phys. Chem. Chem. Phys. **12**, 9751 (2010).

[47] C. Cohen-Tannoudji, J. Dupont-Roc, and G. Grynberg, *Atom-Photon Interactions* (Wiley, New York, 1992).

[48] L. J. Rogers, M. W. Doherty, M. S. J. Barson, S. Onoda, T. Ohshima, and N. B. Manson, New J. Phys. **17**, 013048 (2015).

[49] G. Davies, J. Phys. C **12**, 2551 (1979).

[50] For example, the Ham effect in spin resonance: F. S. Ham, Phys. Rev. **138**, A1727 (1965).